Comparison of water cloud microphysics over mid-latitude land and ocean using CloudSat and MODIS observations

Kazuaki Kawamoto*

Graduate School of Fisheries Science and Environmental Studies, Nagasaki University, Nagasaki, Japan

Kentaroh Suzuki

Jet Propulsion Laboratory, California Institute of Technology, Pasadena, California, USA

**Corresponding author address:* Kazuaki Kawamoto, Graduate School of Fisheries Science and Environmental Studies, Nagasaki University, 1-14 Bunkyo-machi, Nagasaki, Japan 852-8521.

E-mail: kazukawa@nagasaki-u.ac.jp

ABSTRACT

The microphysical properties and processes of water (liquid-phase) clouds in the mid-latitudes were studied using space-borne radar and radiometer data, with a focus on comparisons between continental (over China) and oceanic (over the northwest Pacific) clouds. The probability distribution functions (PDFs) of cloud parameters were examined and found to be both reasonable and consistent with previous observations. The PDFs of oceanic cloud parameters as a function of radar reflectivity were generally better defined than those of land cloud parameters. Precipitation characteristics were categorized into non-precipitating, drizzle, and precipitating, as well as the total-precipitating category, according to the maximum radar reflectivity within the cloud layer. The fractional occurrence of the precipitation categories was analyzed as a function of the liquid water path. The statistics showed general trends that were very similar for both land and oceanic clouds, such as a monotonically decreasing trend for the non-precipitating category, a convex shape for the drizzle category, and a monotonically increasing trend for the precipitating and total-precipitating categories with increasing liquid water path. The fractional occurrence of the precipitation categories was further investigated as a function of multiple cloud parameters to better understand land–ocean contrasts in cloud development stages. The vertical structure of clouds also revealed that oceanic clouds produced heavier precipitation in optically thicker regions, compared to land clouds with fewer cloud droplets. However, the differences between land and oceanic clouds were small when comparisons included only those clouds with a high density of droplets.

1 Introduction

Clouds play a crucial role in Earth's radiation budget. For example, small changes in cloud albedo, vertical distribution, and lifetimes can have a significant impact on the distribution of radiative heating around the globe [1]. Moreover, the various combinations of optical properties among clouds, aerosols, and water vapor create complicated effects on radiation processes [2]. In addition to the radiative effects, clouds also affect the water cycle through precipitation. It is therefore important to improve our understanding of the frequency and magnitude of precipitation in warm clouds [3].

These climatic effects of clouds are also complicated by their interactions with aerosols through the so-called aerosol indirect effect. An increase in the aerosol concentration acts to increase cloud condensation nuclei. The increased number of the condensation nuclei creates smaller and more numerous cloud droplets, which lead to higher cloud reflectivity when the liquid water content is fixed [4]. The decrease in the cloud droplet size also inhibits precipitation and consequently increases the cloud lifetime [5]. In addition, Hansen et al. [6] introduced the idea of the aerosol semi-direct effect in which radiative absorption by aerosols heats the surrounding atmosphere, causing atmospheric stratification that results in a reduction in cloud cover. Huang et al. [7] observationally found that the semi-direct effect of dust aerosols warmed clouds, increased the evaporation of cloud droplets and further reduced the cloud water path. The interaction of aerosols and clouds through these mechanisms still remains one of the most uncertain processes in the climate system [8].

To overcome such a difficulty in understanding the cloud processes and their interaction with aerosols, observations of clouds are crucial. Among various observational tools, satellite-borne instruments are particularly promising for monitoring wide areas with high spatial and temporal resolutions. Passive radiometers, such as the Advanced Very High Resolution Radiometer (AVHRR), have retrieved important cloud microphysical data for several decades. Using these data, Han et al. [9] and Nakajima and Nakajima [10] completed near-global and wide-area analyses, respectively, measuring the cloud optical depth (τ_c) and effective particle radius (r_e) with non-absorbing (0.6-μm) and water-absorbing (3.7-μm) channels. The subsequent Moderate Resolution Imaging Spectroradiometer (MODIS) extended retrieval capabilities, employing 36 channels from the ultraviolet to infrared wavelengths.

More recently, active remote sensing data have become available, such as those from the CloudSat satellite. Launched in April 2006, CloudSat carries the Cloud Profiling Radar (CPR), operating at 94 GHz. A synergetic approach using both active (e.g., CloudSat) and passive (e.g., MOSIS) instruments, such as in the A-Train satellite constellation [11], is an extremely powerful tool in revealing the detailed vertical droplet structures inside clouds, which were previously unknown. A method that combines the radar reflectivity (Z_e) inside the cloud layer from CloudSat with the τ_c of the whole cloud layer, as well as r_e near the cloud top from MODIS, has been devised and used by several previous studies. For example, Lebsock et al. [12] reported aerosol effects on Z_e, the liquid water path (LWP), and r_e over global oceans. Suzuki and Stephens [13] found sixth-power and cubic relationships between Z_e and the effective particle radius of oceanic clouds, illustrating that condensation and coagulation constituted the dominant particle-growth processes at smaller and larger Z_e values, respectively. Furthermore, Nakajima et al. [14] and Suzuki et al. [15] devised a way of combining the vertical profile of Z_e with r_e values derived from MODIS 2.1-μm and 3.7-μm channels to examine particle-growth processes occurring within the cloud layer.

There have been, however, relatively few analyses of clouds over land, mainly owing to the more complicated surface conditions and the unavailability of microwave retrievals over land. Among the studies that have analyzed clouds over land, Kawamoto and Suzuki [16] (hereafter KS12) analyzed the microphysical transition of cloud particles into raindrops in single-layered water clouds over continental regions such as the Amazon and China. Their work was motivated by that of Kawamoto [17], who studied the relationship between cloud properties obtained from passive satellite remote sensing and precipitation rates collected by surface-based rain gauges. KS12 reported the fractional occurrence of precipitation categories defined with Z_e as a function of the LWP, τ_c and r_e behaviors according to precipitation categories, and the behavior of vertical cloud structures as dictated by the CloudSat radar profile information of Z_e.

As an extension from KS12 that was focused on continental clouds, the specific aim of the present study is to compare the properties and characteristics of land and oceanic clouds in an attempt to identify the similarities and differences between them. For this purpose, we combined the observations from the active radar of CPR on-board CloudSat with those from the passive radiometer of MODIS on-board Aqua, in a manner similar to the study of KS12. We investigated several aspects of the cloud-to-precipitation transitional processes inside clouds over land (within 1000 km from 35°N and 105°W over China) and ocean (within 1000 km from 35°N and 165°E over the northwest Pacific) regions at mid-latitudes, which are indicated in Figure 1. These regions were chosen because they are adjacent and nearly continuous over the same latitudes, and therefore are suitable for the comparison analysis of land-ocean contrasts in mid-latitude water (liquid-phase) clouds. In this study, we confine our analyses to low-level water clouds because of their large area of coverage and substantial radiative effect. To avoid the complexity that arises from multi-layered clouds, we selected only single-layered clouds.

The remainder of this paper is arranged as follows. In Section 2, we briefly described the datasets used. Section 3 presented the main analyses conducted, specifically the probability distribution function (PDF) of cloud parameters, PDF of cloud parameters as a function of Z_e, the fractional occurrences of precipitation categories as a function of the LWP, the fractional occurrences of precipitation categories as a function of multiple cloud parameters in the context of their two-dimensional representations, and the transitional characteristics of cloud vertical structures as a function of τ_c and Z_e according to the cloud droplet number density (N_c). Finally, Section 4 summarized the findings and conclusions of this study.

2 Datasets

We used the same five cloud parameters as used by KS12 to investigate the precipitation characteristics in clouds formed over land and ocean: τ_c, r_e, LWP, N_c, and Z_e. The τ_c and r_e data were retrieved from the MODIS visible (non-absorbing) 0.6-µm and near-infrared (absorbing) 2.1-µm channels, and these values were taken from the CloudSat 2B-TAU product which only took MODIS pixels that were collocated with the CloudSat footprint [18]. This study used data with uncertainties less than 3 for τ_c and less than 1 µm for r_e. The LWP and N_c values were derived from the τ_c and r_e retrievals according to the adiabatic growth assumption: the LWP was calculated as $5\tau_c r_e/9$ [19] and N_c was estimated using equation (1) below, which was originally equation (3) of Kubar *et al*. [20]:

$$N_c=\sqrt{2}\, B^3\Gamma_{\mathrm{eff}}^{\ 1/2}\mathrm{LWP}^{1/2}/\ r_e^{\ 3}, \qquad (1)$$

where $B = (3\pi\rho_w/4)^{1/3} = 0.0620$, ρ_w is the density of liquid water, and Γ_{eff} is the adiabatic rate of increase in the liquid water content with height. Γ_{eff} is weakly dependent on pressure and temperature and was derived from a diagram by Wood [21]. Taking the uncertainties less than 3 for τ_c and less than 1 µm for r_e into account, uncertainties of the inferred LWP and N_c were generally estimated to less than 20 (g/m^2) and 25 (1/cm^3), respectively. Z_e was obtained from the CloudSat 2B-GEOPROF product [22,23]. In addition, altitude and temperature profiles were obtained from the European Centre for

Medium-Range Weather Forecasts Auxiliary (ECMWF-AUX) dataset matched to the CloudSat radar footprint [24].

We used the CloudSat data mentioned above, collocated with MODIS products for the periods of June, July, August (JJA) and December, January, February (DJF) from 2006 to 2008, to examine the averaged behaviors of single-layered water clouds over these seasons in mid-latitudes.

3. Results

3.1 Selection of single-layered water clouds

Only single-layered and water (liquid-phase) clouds having $\tau_c > 1$ and $r_e < 35$ (μm) were selected to reduce retrieval error in the products. The single-layered requirement was determined as follows, according to the method of Haynes and Stephens [25]. First, moving upward from the lowest layer, *i.e.*, the closest to the ground, we examined whether layers met the following three conditions: (1) the cloud mask value was between 30 and 40; (2) Z_e was not an undefined value; and (3) the height value was positive. The first height bin that satisfied all of the conditions was defined as the cloud base. Next, we examined the layers upward from the cloud base, and the bins that satisfied all of the conditions were determined to be the cloud layer. The layer just under the first layer not satisfying these conditions was defined as the "cloud top of the lower layer" (CTL). The same procedure was then conducted downward from the highest layer, and the first layer that satisfied all the conditions was called the "cloud top of the higher layer" (CTH). If CTL and CTH were identical, we considered the cloud layer to be single-layered. Otherwise, we concluded that the atmospheric column consisted of multilayered clouds. The latter (liquid-phase) requirement was identified by the CloudSat cloud mask criterion and an echo-top temperature warmer than 273K. We compared our cloud phase identification with the information of the 2B-CWC-RVOD product, which combined MODIS and CloudSat data. The results showed that 81.1% of our estimation of water agreed with the 2B-CWC-RVOD product over land and 75.2% agreed over ocean.

3.2 Probability distribution functions (PDFs) of cloud parameters

To investigate the overall characteristics of clouds, we first constructed PDFs of cloud parameters (τ_c, r_e, LWP, N_c, and Z_e) over land and ocean, as shown in Fig. 2. Figure 2(a) shows that both land and oceanic clouds had a similar PDF of τ_c, whose mode value was about 25, indicating that land clouds were slightly thicker optically. Figure 2(b) shows that oceanic clouds had distinctly larger r_e than did land clouds and this difference was significant judging from the uncertainty of 1 μm considered in this study. Oceanic clouds had a higher mode value of the LWP than did land clouds, caused by larger values of r_e (Figure 2(c)). Conversely, land clouds had definitely more N_c than oceanic clouds (Figure 2(d)). This land–ocean contrast and the mode values of N_c are reasonable and comparable to results from past aircraft measurements (*e.g.*, [26]). The land-ocean contrast found in N_c may reflect a signature in aerosol abundance, as supported by MODIS-retrieved aerosol optical depth (AOD) annual-mean values [27], which were estimated as 0.45 and 0.18 over land (characterized by industrial and dust aerosols) and ocean (less influenced by anthropogenic sources), respectively. These features are also those expected from the Twomey's theory [4] and consistent with results of previous observational studies (e.g., [28]). Also shown in Figure 2(e) is the PDF of Z_e for all the cloud layers. It was found that both land and oceanic clouds had bimodal characteristics, and the mode value for oceanic clouds (roughly 2 dBZ) was larger than that of land clouds (roughly -8 dBZ). Also, oceanic clouds showed a higher frequency of Z_e > -5dBZ than did land clouds, and vice versa. These features of land and oceanic clouds are similar to those reported by KS12 for clouds over China and the Amazon, respectively.

For studying how these characteristics of cloud properties were related to precipitation processes, the cloud-to-rain transition processes were analyzed in terms of precipitation categories defined according to the maximum Z_e value within the cloud layer. The precipitation categories were defined with threshold values as follows: (i) non-precipitating (Z_e < –15 dBZ); (ii) drizzle (–15 dBZ < Z_e < 0 dBZ), and (iii) precipitating (0 dBZ < Z_e), following Suzuki et al. [29]. L'Ecuyer et al. [1] further divided the drizzle category into two subcategories of drizzle (–15 dBZ < Z_e < –7 dBZ) and light rain (–7 dBZ < Z_e < 0 dBZ), although that classification was not used here. In addition to the three categories above, we also introduced the category of total-precipitating events

(–15 dBZ < Z_e) as combined category of the drizzle and precipitating categories defined above. These four categories are hereafter referred to as Z_e1, Z_e2, Z_e3, and Z_e4, respectively. The two threshold values of -15 and 0 dBZ dividing these categories were superimposed in Figure 2(e). Although Suzuki et al. [29] utilized near-surface non-attenuated radar reflectivity from the *CloudSat* 2C-PRECIP-COLUMN data available only over the ocean, we used the maximum radar reflectivity within the cloud layer for consistent analyses over both land and ocean.

3.3 PDFs of cloud parameters as a function of Z_e

Next, we analyzed the PDFs of cloud parameters as a function of Z_e to examine how they tend to change with changing Z_e, taking Z_e as the horizontal coordinate and the PDFs of cloud parameters as the vertical coordinate. Figures 3 (a)–(d) and 4 (a)–(d) illustrate the results over land and ocean for τ_c, r_e, LWP, and N_c, respectively. First, the tendencies of oceanic cloud parameters showed generally better-defined relationships with Z_e values, such as a negative relationship of N_c and positive relationships of τ_c, r_e, and LWP as Z_e increased with saturation for Z_e > 0 dBZ. Land clouds showed the same tendencies, except for the flat variation in τ_c, but the tendencies were particularly less distinct for Z_e > 0 dBZ. The less distinct tendencies of land cloud parameters for this region might be partly due to the small number of samples, as shown in Fig. 2(e).

It should be noted that the LWP and N_c are by-products and are not independent of τ_c and r_e. We used the LWP obtained from τ_c and r_e in the present study for consistent analyses over both land and ocean. It would be of interest in future studies to apply the same procedure to microwave-derived LWP values, which would be independent of optical measurements, for a comparison of oceanic cloud behavior since the microwave retrievals are available only over the ocean.

3.4 Fractional occurrence of precipitation categories as a function of the LWP

We analyzed the fractional occurrences of the four categories (Z_{e1}–Z_{e4}) as a function of the LWP and the results are shown in Fig. 5. In this study, the fractional occurrence was calculated as the ratio of the number of samples that satisfied the condition to the total number of samples in the bin. Note that the PDF is not shown in Fig. 5(a)–(d), unlike in Fig. 2(a)–(e). Lebsock *et al*. [12] found that the probability of precipitation, defined as the fractional occurrence of precipitation events, increased monotonically with the LWP for oceanic clouds. In Fig. 5(a) through (d), the fractional occurrences of non-precipitating, drizzling, precipitating, and total-precipitating categories are shown as a function of the LWP for land and oceanic clouds. Figure 5(a) presents monotonically decreasing trends for both land and oceanic clouds in the non-precipitating category. Land clouds had higher frequencies of the non-precipitating category than oceanic clouds for LWP from 100 to 500 (g/m^2). At LWP > 500 (g/m^2), a majority of clouds were either drizzling or precipitating. For the drizzling category (Fig. 5(b)), convex shapes are found for both land and ocean clouds, but the peak LWP was considerably larger for land clouds (about 400 g/m^2) than for oceanic clouds (about 200 g/m^2); the smaller particle sizes over land may have resulted in the larger frequency of drizzle compared to the precipitating category (Fig. 5(c)) as argued below. In Fig. 5(c) showing the precipitating category, both land and ocean clouds have monotonically increasing trends, but higher frequencies are found over LWP from 100 to 650 (g/m^2) for oceanic clouds than land clouds that tend to have larger LWP values for the precipitation frequency to reach the comparable value to oceanic clouds. At LWP > 650 (g/m^2), all clouds approached unity. In addition, the total-precipitating category in Fig. 5(d) shows a monotonically increasing trend. Although in general the precipitation frequency was higher in oceanic clouds than land clouds, the clouds over both areas were precipitating at LWP > 500 (g/m^2), consistent with the interpretation of Fig. 5(a) for the non-precipitating category.

These behaviors of land clouds tend to be similar to those previously found in polluted coastal areas (*e.g.*, Asian coast and Gulf of Mexico) by Kubar *et al*. [20] (see their Fig. 11(b)). Conversely, the behavior of oceanic clouds fell in between those of clouds in polluted coastal areas and the remote oceanic area reported by Kubar *et al*. [20] (also see their Fig. 11(b)) because the oceanic area in this study was relatively near the East Asian coast.

3.5 Fractional occurrences of precipitation categories using a two-dimensional plane

In this sub-section, the fractional occurrences of precipitation categories are further studied by the two-dimensional representations of τ_c–r_e and LWP–N_c combinations, according to the method of Suzuki et al. [29]. As those authors stated, such an analysis provides a more detailed examination of warm rain formation than Figure 5 in terms of cloud properties in the two-dimensional representation, making the maximum use of the MODIS cloud retrievals.

Figure 6 shows fractional occurrences of precipitation categories as a function of τ_c and r_e over land (a–c) and ocean (d–f). The overall behaviors of the contributions of τ_c–r_e to differences between non-precipitating and precipitation categories were similar between land and oceanic clouds. For example, the non-precipitating category generally occurs in the region of small τ_c with broad r_e values and small r_e with broad τ_c values, showing an L-like shape. The drizzle category mainly appears over the intermediate region between larger τ_c and smaller r_e to smaller τ_c and larger r_e. The precipitating category occupies the remaining upper-right region having larger τ_c and r_e values. Nevertheless, the precipitation category displays greater differences between land and oceanic clouds when compared to the other categories, such as greater frequencies of the precipitating category over larger values of τ_c and r_e for oceanic clouds. It should be noted that the parameters of regional analyses such as ours, which do not cover the entire plane, are inherently different from those of Suzuki et al. [29], who have conducted global ocean analyses.

Figure 7 shows fractional occurrences of the precipitation categories as a function of LWP and N_c over land (a–c) and ocean (d–f). The non-precipitating category was shown to occur generally over small LWP with broad N_c values. The drizzle category was found to take place over larger LWP and smaller N_c than the non-precipitating category. The precipitating category was shown to occur in the lower-right region of the N_c -LWP plane, corresponding to larger LWP and smaller N_c. As in the τ_c–r_e case, the precipitation characteristics in terms of the LWP–N_c plane are similar between land and oceanic clouds, although land clouds have smaller N_c values than oceanic clouds. For both the τ_c–r_e and LWP–N_c cases, fractional frequencies of the precipitation categories are systematically shifted among non-precipitating, drizzle, and precipitating categories. As pointed out by Suzuki et al. [29], this approach can reveal how cloud properties contribute to each precipitation category, and how they tend to systematically vary among each precipitation category.

3.6 Vertical structure shown by a contoured frequency by optical depth diagram (CFODD)

By combining the specific attributes of CloudSat and MODIS data, detailed vertical features and structures of cloud microphysical process can be revealed as previously reported by Nakajima et al. [14] and Suzuki et al. [15]. These studies offered a new diagram called the contoured frequency by optical depth diagram (CFODD) using optical depth as the vertical coordinate, instead of geometric height, to describe the vertical profile of the radar reflectivity, which is taken as the horizontal coordinate. Suzuki et al. [15] utilized the cloud adiabatic model to distribute in-cloud optical depth from the total optical depth determined from MODIS shortwave radiances, providing a vertical slicing of the optical depth in a manner independent of the radar reflectivity profile information. We adopted this CFODD approach to investigate the vertical structures of water clouds over land and ocean. We classified CFODDs according to N_c to directly interpret the relationships of cloud parameters in the context of the aerosol indirect effect, following KS12. This approach differs from those of Nakajima et al. [14] and Suzuki et al. [15], who classified CFODDs according to r_e. To examine the transitional characteristics of cloud vertical profiles, three N_c categories, referred to as N_1, N_2, and N_3, were introduced to correspond with higher, moderate, and lower cloud droplet number populations, respectively. Thresholds of 80 cm^{-3} and 120 cm^{-3} were used to divide these categories for both land and oceanic cloud analyses.

The CFODDs for N_1, N_2, and N_3 are shown in Fig. 8(a–c) and (d–f) for measurements over land and ocean, respectively. Overall, the main features describing a transition from N_1 to N_3 were similar between oceanic and land clouds. More specifically, high-frequency regions shifted to a larger Z_e and a smaller τ_c as N_c decreased from N_1 to N_3. KS12 interpreted this phenomenon as follows: after the cloud development stage, N_c

decreases and r_e increases through coalescence, resulting in a decrease in τ_c due to a reduction in the total cross-section of particles. Moreover, the total water within clouds decreases with precipitation events. Evaporation might also decrease the particle size and eliminate particles, both of which result in τ_c decreasing via liquid water loss. Figure 8(a) and Fig. 8(d) for the N_1 case are generally similar and frequent at smaller Z_e. Figure 8(b) and Fig. 8(e) of the N_2 case are also similar, moving to slightly larger Z_e than the N_1 case. As for the N_3 case, Fig. 8(f) shows that oceanic clouds are more frequent in optically thicker and larger Z_e regions, which suggests more precipitation, compared to the land clouds shown in Fig. 8(c). A larger Z_e corresponds to larger r_e, which is consistent with the larger r_e of oceanic clouds. Moreover, the N_3 cases are even more different from the N_1 and N_2 cases, particularly for oceanic clouds.

4 Conclusions

Following KS12, who analyzed water cloud microphysical and transitional processes over the Amazon and China using a combination of both active radar (CloudSat) and passive radiometer (MODIS) data, we applied the same analysis approach to mid-latitude water clouds to examine land–ocean differences in relationships among cloud droplets, drizzle, and precipitation. The cloud parameters used were τ_c and r_e from MODIS; LWP and N_c as by-products of τ_c and r_e; and Z_e from CloudSat. We analyzed the following parameters with the synergistic use of active CloudSat and passive MODIS data: 1) PDFs of cloud parameters, 2) PDFs of cloud parameters as a function of Z_e, 3) fractional occurrences of precipitation categories as a function of the LWP, 4) fractional occurrences of precipitation categories as a function of τ_c and r_e, and of the LWP and N_c, and 5) vertical cloud structure using CFODD.

The PDFs of cloud optical and microphysical parameters were reasonable and consistent with previous studies, such that r_e was smaller and N_c was larger for land clouds. These results support Twomey's idea regarding the differences in aerosol abundance between land and ocean. Although the distributions of τ_c were similar between land and oceanic clouds, LWP was larger for oceanic clouds owing to larger values of r_e. For the PDF of Z_e, both land and oceanic clouds had bimodal shapes. We also found that the oceanic clouds had a larger mode of Z_e and higher frequencies at the larger Z_e range. Then, we classified the precipitation characteristics into the four categories non-precipitating, drizzle, precipitating, and total-precipitating, using the thresholds of –15 and 0 dBZ to divide categories. Next, we analyzed the PDFs of cloud parameters as a function of Z_e in order to examine how they tend to change with changing Z_e, taking Z_e as the horizontal coordinate and the PDFs of cloud parameters as the vertical coordinate. Figures 3 (a)–(d) and 4 (a)–(d) illustrate the results over land and ocean for τ_c, r_e, LWP, and N_c, respectively. Although monotonic trends were observed for both land and oceanic cloud parameters, such as positive trends of τ_c, r_e, and LWP and a negative trend of N_c, on the whole, land cloud parameters showed less distinct trends for $Z_e > 0$ dBZ. Then, the fractional occurrences of these precipitation categories were examined as a function of the LWP (Fig. 5). General trends were found to be very similar between land and oceanic clouds, such as a monotonically decreasing trend in the non-precipitating, a convex shape for the drizzle, and monotonically increasing trends of both the precipitating and total-precipitating categories. Although both land and oceanic clouds showed the convex shape for the drizzle category, the peak value of LWP was larger for land clouds, implying that more cloud water is required for drizzle particles to form over land than over ocean because of smaller cloud droplets over land. The same tendencies were also found in the precipitating category that shows larger LWP values over land for the fractional occurrence to reach the same value as over ocean.

We further analyzed the fractional occurrences of the precipitation categories in terms of two-dimensional representations of cloud parameters, such as combinations of τ_c–r_e and LWP–N_c, instead of the LWP alone. Systematic changes in the transition regarding pairs of the cloud parameters were captured well for all precipitation categories. The transition pattern was generally similar between land and oceanic clouds. As Suzuki *et al*. [29] suggested, use of this two-dimensional method can reveal the detailed characteristics of cloud parameters and fractional occurrences of each precipitation category. Finally, the CFODD diagram, with τ_c as the vertical coordinate and Z_e as the horizontal coordinate, was used to classify cloud development stages in terms of N_c. This CFODD approach may also reveal the transitional characteristics of cloud vertical structure. In particular, oceanic clouds were found to produce heavier precipitation from optically thicker regions than land clouds in N_3. This is consistent with Fig. 2(e), which shows that the oceanic clouds had larger modes of Z_e and were more frequent in the larger Z_e range. However, whether a cloud was of land or oceanic origin made little difference in N_1.

At last, let us summarize the discussion on relations among τ_c, r_e, LWP and N_c. The LWP and N_c, which were derived from and were not independent of τ_c and r_e in this study, are important parameters in current analyses such that the LWP is taken as the *x*-axis in fractional occurrences of the precipitation category of Fig. 5, and N_c is used as the threshold in the CFODD of Fig. 8. From the viewpoint of cloud physics, the behaviors of τ_c, r_e, LWP, and N_c so obtained can be summarized as follows. Using the PDFs as a function of the Z_e in Figs. 3 and 4, τ_c, r_e, and the LWP monotonically increase with Z_e, storing water mass inside the cloud layer, while N_c is decreased due to the collision–coalescence process, which produces raindrops and whose temporal progress can be seen from the left to the right in Figures 3 and 4.

Future work regarding this study can be mentioned as follows. It would be useful to extend these kinds of analyses to various locations across the globe, in addition to the mid-latitudes examined in this study, and to determine differences and similarities in microphysical features. Recently, Zhu *et al*. [30] proposed a mechanism for the aerosol concentration increase due to weakening of the East Asian summer monsoon. It would be quite interesting in this context to examine the correlation between the aerosol concentration and precipitating/non-precipitating frequencies over various locations, as well as over East Asia. Furthermore, Lebsock et al. [3] derived vertical profiles of precipitation rate and discussed the ratios of rain and cloud water for oceanic low-level clouds. A vertical analysis of precipitation rate, when combined with the current approach, may help to clarify the transitional processes involved in cloud droplet, drizzle, and precipitation formation inside the cloud layer.

Acknowledgments.

K. Kawamoto was supported by the Mitsui & Co., Ltd., Environment Fund, Grant-in aid for Scientific Research (B) and Grant-in aid for Scientific Research on Innovative Areas. The CloudSat data products of 2B-GEOPROF and MODIS-AUX and ECMWF-AUX were provided by the CloudSat Data Processing Center at CIRA/Colorado State University. Part of the research was carried out at the Jet Propulsion Laboratory, California Institute of Technology, under a contract with the National Aeronautics and Space Administration.

References

[1] L'Ecuyer TS, Berg W, Haynes JM, Lebsock MD, Takemura T. Global observations of aerosol impacts on precipitation occurrence in warm maritime clouds. J Geophys Res 2009;114:D09211, doi:10.1029/2008JD011273.

[2] Kawamoto K, Hayasaka T. Relative contributions to surface shortwave irradiance over China: A new index of potential radiative forcing. Geophys Res Lett 2008;35:L17809, doi:10.1029/2008GL035083.

[3] Lebsock MD, L'Ecuyer TS, Stephens GL. Detecting the ratio of rain and cloud water in low-latitude shallow marine clouds. J Appl Meteor Clim 2011;50:419-432, doi:10.1175/2010JAMC2494.1.

[4] Twomey S. The influence of pollution on the shortwave albedo of clouds. J Atmos Sci 1977;34:1149–52.

[5] Albrecht B. Aerosols, cloud microphysics, and fractional cloudiness. Science 1989;245:1227–30.

[6] Hansen J, Sato M, Ruedy R. Radiative forcing and climate response. J Geophys Res 1997;102:6831–64.

[7] Huang J, Lin B, Minnis P, Wang T, Wang X, Hu Y, Yi Y, Ayers JK. Satellite-based assessment of possible dust aerosols semi-direct effect on cloud water path over East Asia. Geophys Res Lett 2006:33, L19802, doi:10.1029/2006GL026561.

[8] IPCC. Climate Change 2007: The Physical Science Basis, Contribution of Working Group I to the Fourth Assessment Report of the Intergovernmental Panel on Climate Change. Cambridge University Press 2007;996 pp.

[9] Han Q, Rossow WB, Lacis AA. Near-global survey of effective droplet radii in liquid water clouds using ISCCP data. J Clim 1994;7:465–97.

[10] Nakajima TY, Nakajima T. Wide-area determination of cloud microphysical properties from NOAA AVHRR measurements for FIRE and ASTEX regions. J Atmos Sci 1995;52:4043–59.

[11] Stephens GL, et al. The CloudSat mission and the A-Train. Bull Amer Meteor Soc 2002;83:1771–90.

[12] Lebsock MD, Stephens GL, Kummerow C. Multisensor satellite observations of aerosol effects on warm clouds. J Geophys Res 2008;113:D15205, doi:10.1029/2008JD009876.

[13] Suzuki K, Stephens GL. Global identification of warm cloud microphysical processes with combined use of A-Train observations. Geophys Res Lett 2008;35: L08805, doi:10.1029/2008GL033590.

[14] Nakajima TY, Suzuki K, Stephens GL. Droplet growth in warm water clouds observed by the A-Train. Part II: A multi-sensor view. J Atmos Sci 2010;67:1897–1907.

[15] Suzuki K, Nakajima TY, Stephens GL. Particle growth and drop collection efficiency of warm clouds as inferred from joint CloudSat and MODIS observations. J Atmos Sci 2010;67:3019–32.

[16] Kawamoto K, Suzuki K. Microphysical transition in water clouds over the Amazon and China derived from space-borne radar and radiometer data. J Geophys Res 2012;117:D05212, doi:10.1029/2011JD016412.

[17] Kawamoto K, Effect of precipitation on water cloud properties over China. Geophys Res Lett 2008;35:L20811, doi:10.1029/2008GL035052.

[18] Polonsky I, Level 2 cloud optical depth product process description and interface control document. CloudSat Project 2008;CIRA, Colorado State University, Fort Collins, 21 pp. [Available online at http://www.cloudsat.cira.clostate.edu/ICD/2BTAU/2B-TAU_PDICD_5.0.pdf.]

[19] Brenguier J, Pawlowska H, Schuller L, Preusker R, Fischer J, Fouquart Y. Radiative properties of boundary layer clouds: Droplet effective radius versus number concentration. J Atmos Sci 2000;57:803–21.

[20] Kubar TL, Hartmann DL, Wood R. Understanding the importance of microphysics and macrophysics for warm rain in marine low clouds. Part I: Satellite observations. J Atmos Sci 2009;66:2953–72.

[21] Wood R. Relationships between optical depth, liquid water path, droplet concentration, and effective radius in adiabatic layer cloud. University of Washington 2006;3 pp. [Available online at http://www.atmos.washington.edu/;robwood/papers/chilean_plume/optical_depth_relations.pdf.]

[22] Mace GG, Marchand R, Zhang Q, Stephens GL. Global hydrometeor occurrence as observed by CloudSat: Initial observations from summer 2006. Geophys Res Lett 2007;34: L09808, doi:10.1029/2006GL029017.

[23] Marchand R, Mace GG, Ackerman T, Stephens GL. Hydrometeor detection using CloudSat - An Earth-orbiting 94GHz cloud radar. J Atmos Ocean Tech 2008;25:519–33.

[24] Partain P. Cloudsat ECMWF-AUX auxiliary data process description and interface control document. CloudSat Project, CIRA, Colorado State University, Fort Collins 2007;10 pp. [Available online at http://www.cloudsat.cira.colostate.edu/dataICDlist.php?go=list&path=/ECMWF-AUX]

[25] Haynes JM, Stephens GL. Tropical oceanic cloudiness and the incidence of precipitation: Early results from CloudSat. Geophys Res Lett 2007;34:L09811, doi:10.1029/2007GL029335.

[26] Gultepe I, Isaac GA. Aircraft observations of cloud droplet number concentration: Implications for climate studies. Q J R Meteorol Soc 2004;130:2377–90.

[27] Remer LA, et al. The MODIS aerosol algorithm, products and validation. J Atmos Sci 2005;62:947–73.

[28] Kawamoto K, Nakajima T, Nakajima TY. A global determination of cloud microphysics with AVHRR remote sensing. J Clim 2001;14:2054– 68.

[29] Suzuki K, Stephens GL, van den Heever SC, Nakajima TY. Diagnosis of the warm rain process in cloud-resolving models using joint CloudSat and MODIS observations. J Atmos Sci 2011;68:2655-70.

[30] Zhu J, Liao H, Li J. Increases in aerosol concentrations over eastern China due to the decadal-scale weakening of the East Asian summer monsoon. Geophys Res Lett 2012:*39*, L09809, doi:10.1029/2012GL051428.

Figure captions

Figure 1. Map of the regions analyzed in this study. The solid and dotted circles represent the land areas (within 1000 km from 35°N and 105°W over China) and oceanic areas (within 1000 km of 35°N and 165°E over the northwest Pacific) included, respectively.

Figure 2. Probability distribution functions of (a) τ_c, (b) r_e, (c) LWP, (d) N_c, and (e) Z_e for land and oceanic clouds. The two threshold values of -15 and 0 (dBZ) were imposed in Fig. 2(e).

Figure 3. Probability distribution functions of (a) τ_c, (b) r_e, (c) LWP and (d) N_c as a function of Z_e for land clouds.

Figure 4. As in Fig.3, but for oceanic clouds.

Figure 5. Fractional occurrences of (a) non-precipitating, (b) drizzle, (c) precipitation, and (d) total-precipitation as a function of the LWP for land and oceanic clouds.

Figure 6. Fractional occurrences of (a) non-precipitating, (b) drizzle, and (c) precipitation as a function of τ_c and r_e for land and oceanic clouds.

Figure 7. As in Fig.6, but as a function of LWP and N_c

Figure 8. CFODDs of the (a) land clouds for N_1, (b) land clouds for N_2, (c) land clouds for N_3, (d) oceanic clouds for N_1, (e) oceanic clouds for N_2 and, (f) oceanic clouds for N_3.

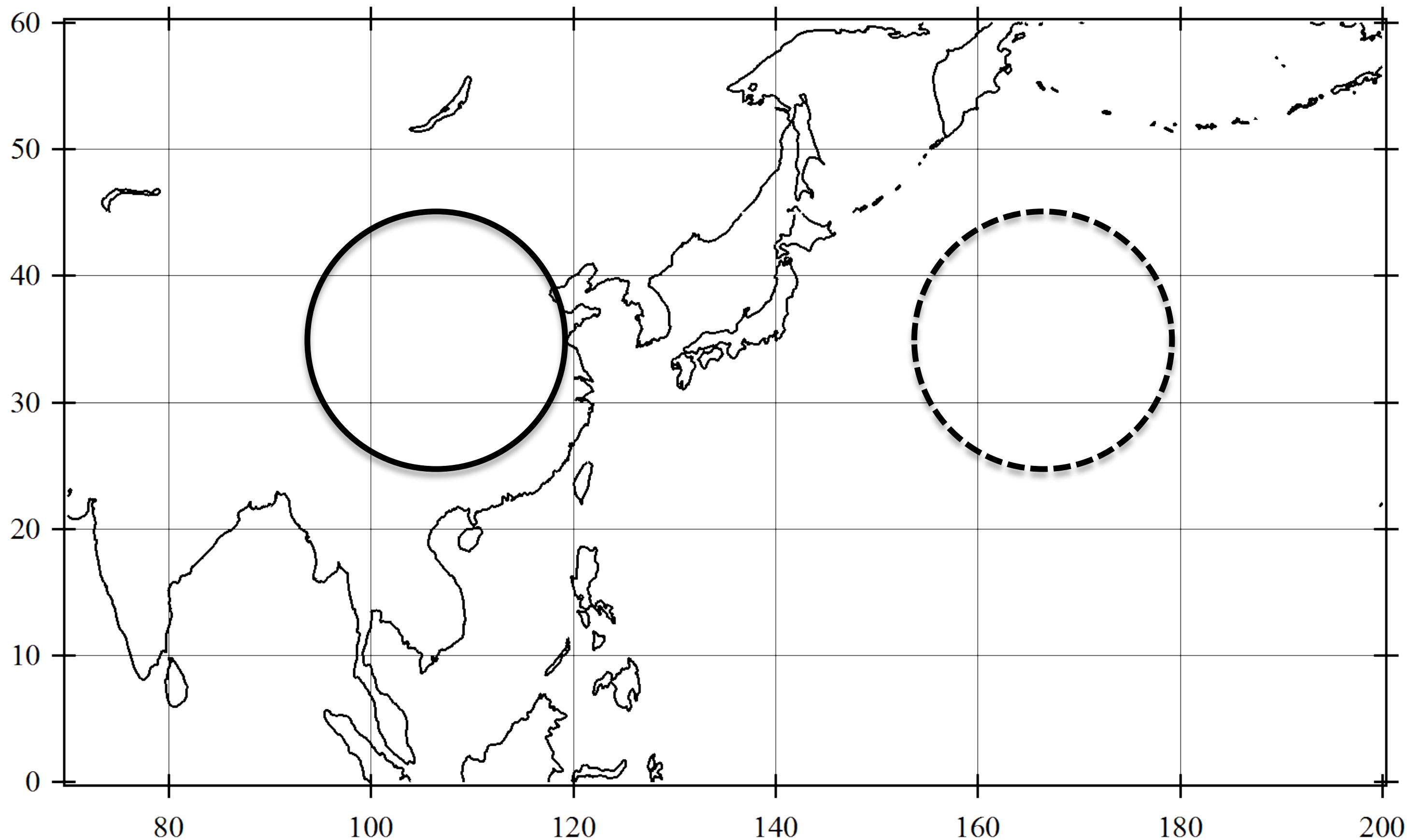

Fig.1

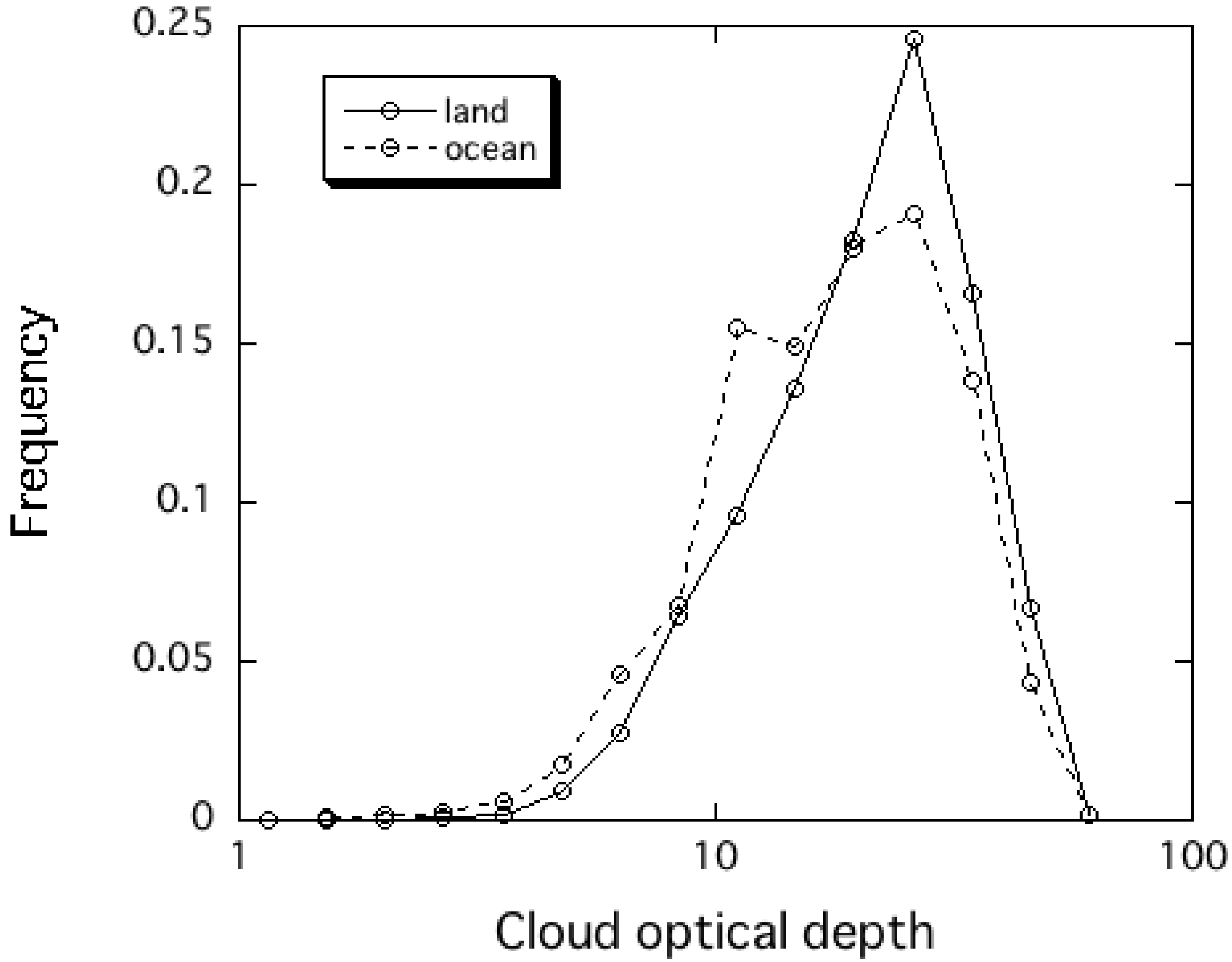

0.25
0.2
0.15
0.1
0.05
0
Frequency
land
ocean
1
10
100
Cloud optical depth

Fig.2 (a)

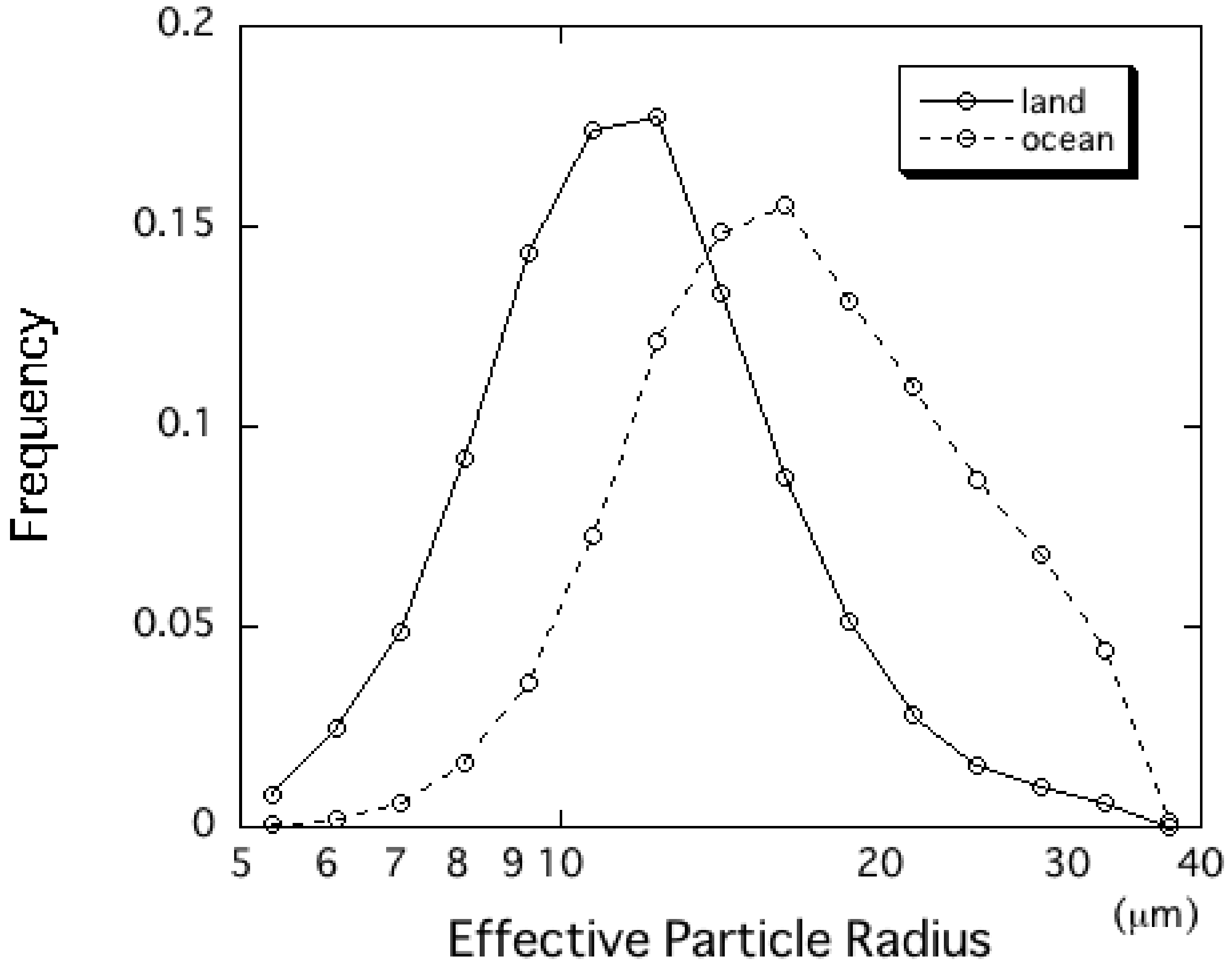
0.2
0.15
0.1
0.05
0
Frequency
land
ocean
5
6
7
8
9
10
20
30
40
(μm)
Effective Particle Radius

Fig.2 (b)

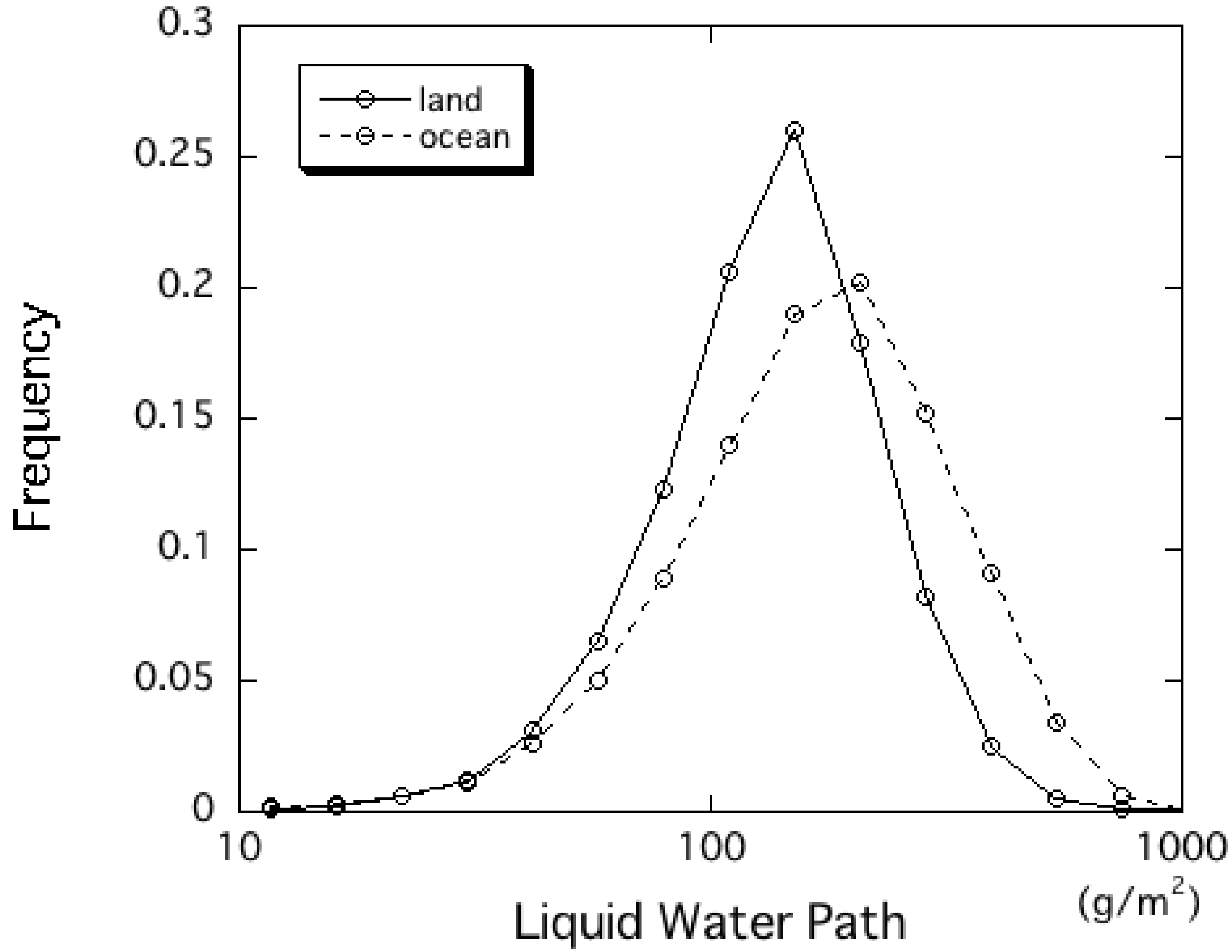

0.3
0.25
0.2
0.15
0.1
0.05
0
Frequency
land
ocean
10
100
1000
(g/m^2)
Liquid Water Path

Fig.2 (c)

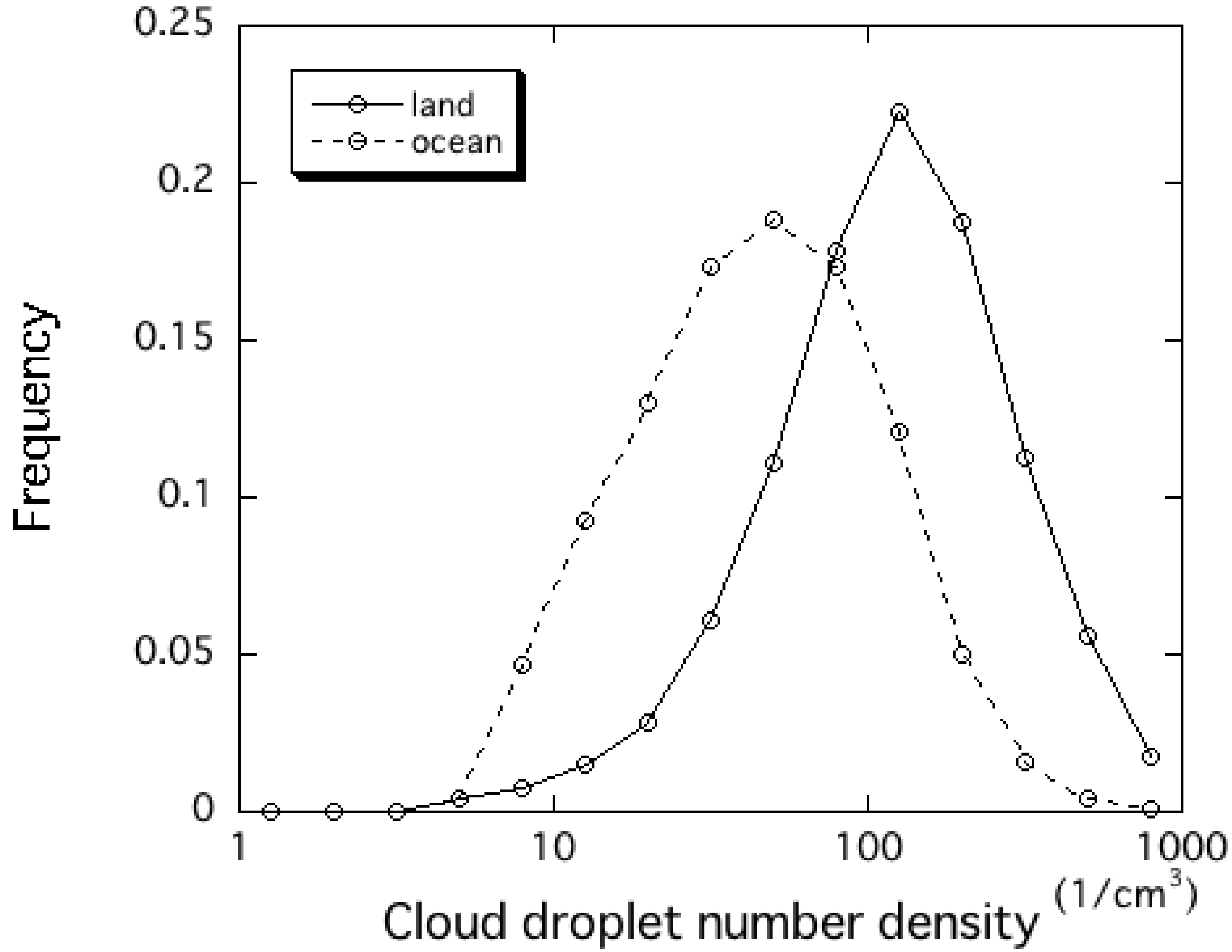

0.25
0.2
0.15
0.1
0.05
0
Frequency
1
10
100
1000
Cloud droplet number density
(1/cm³)
land
ocean

Fig.2 (d)

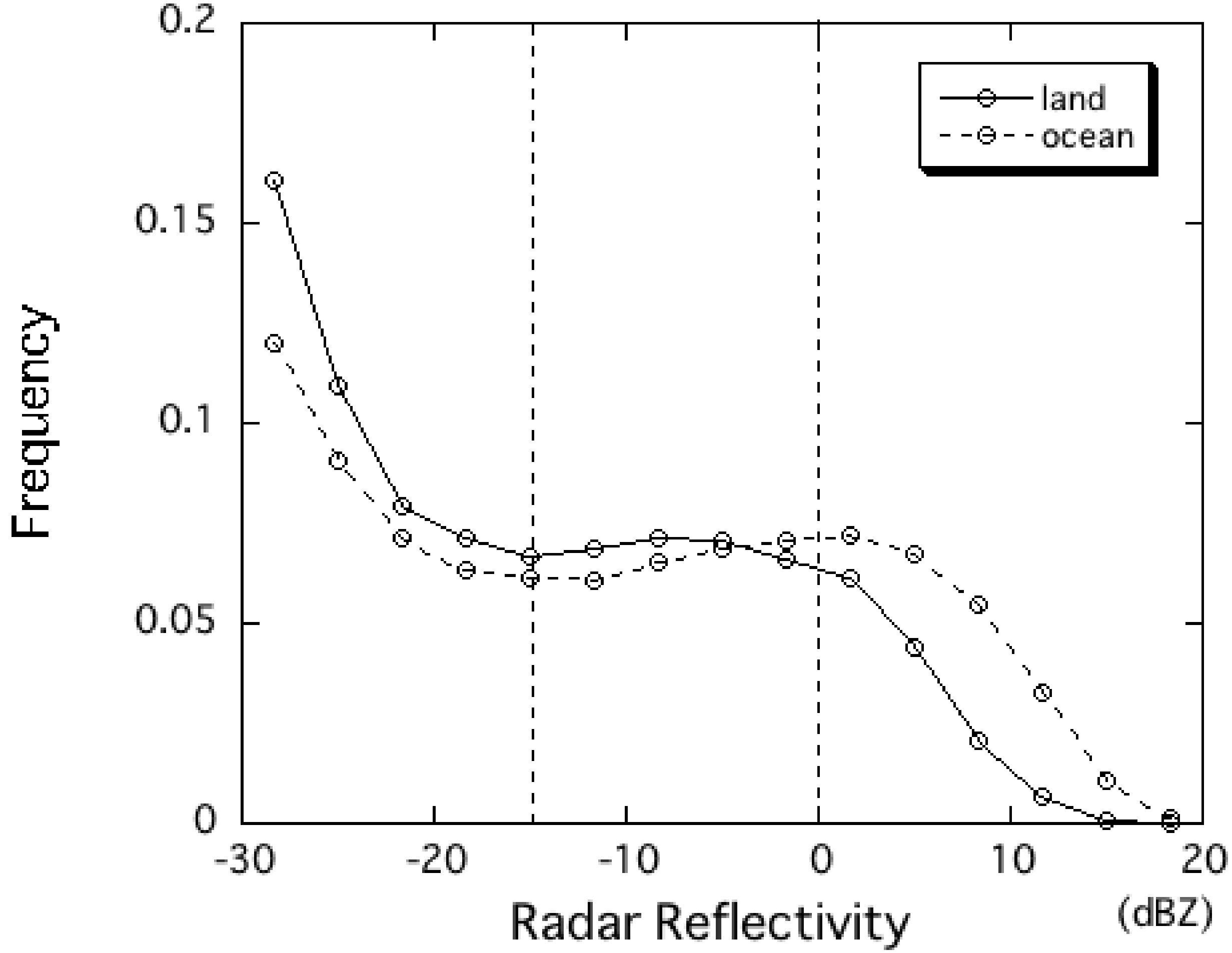

0.2
0.15
0.1
0.05
0
Frequency
-30
-20
-10
0
10
20
Radar Reflectivity
(dBZ)
land
ocean

Fig.2 (e)

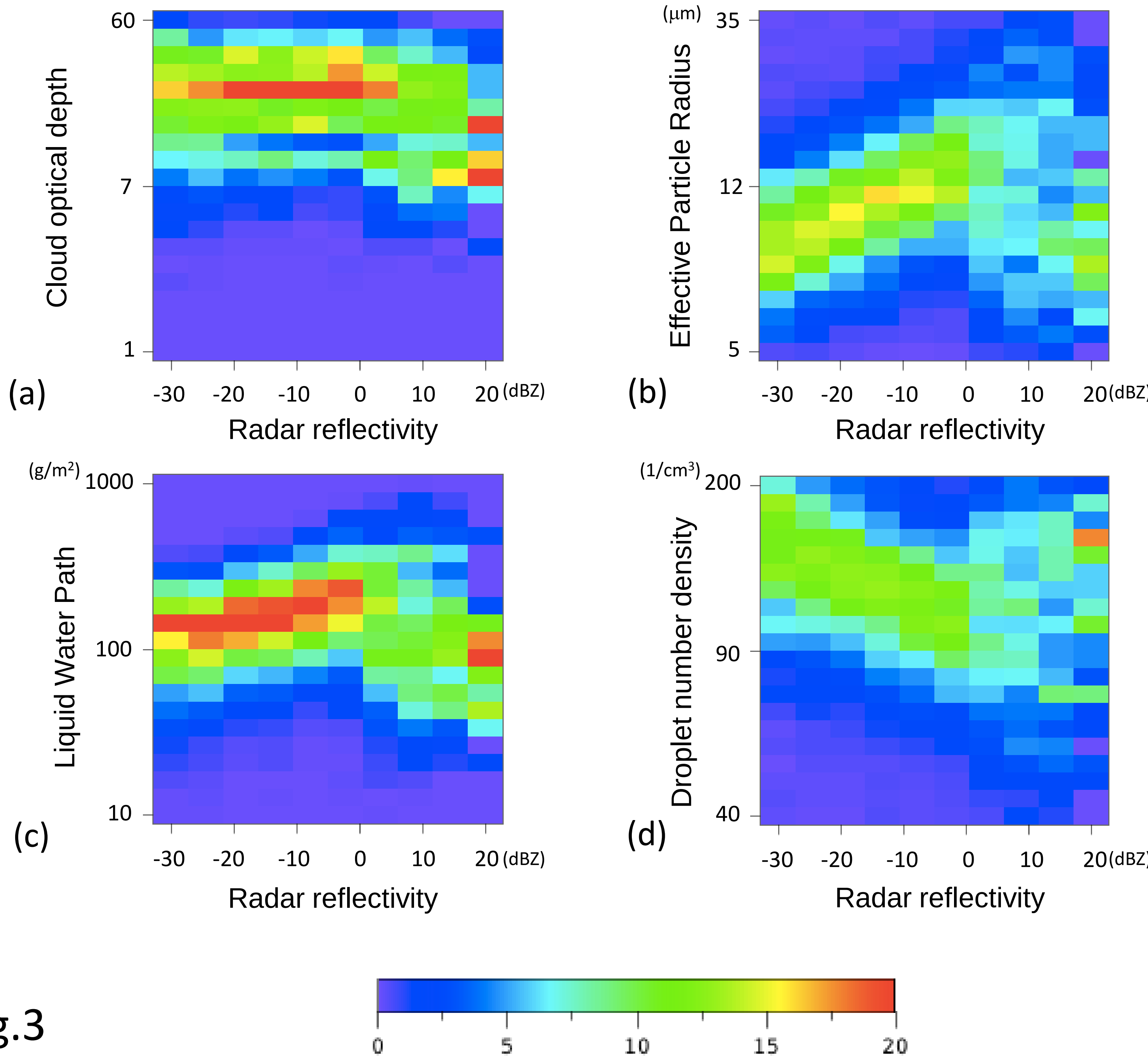

(a)
Cloud optical depth
60
7
1
-30
-20
-10
0
10
20
(dBZ)
Radar reflectivity
(b)
Effective Particle Radius
(μm)
35
12
5
Radar reflectivity
(c)
Liquid Water Path
(g/m²)
1000
100
10
Radar reflectivity
(d)
Droplet number density
(1/cm³)
200
90
40
Radar reflectivity
0
5
10
15
20

Fig.3

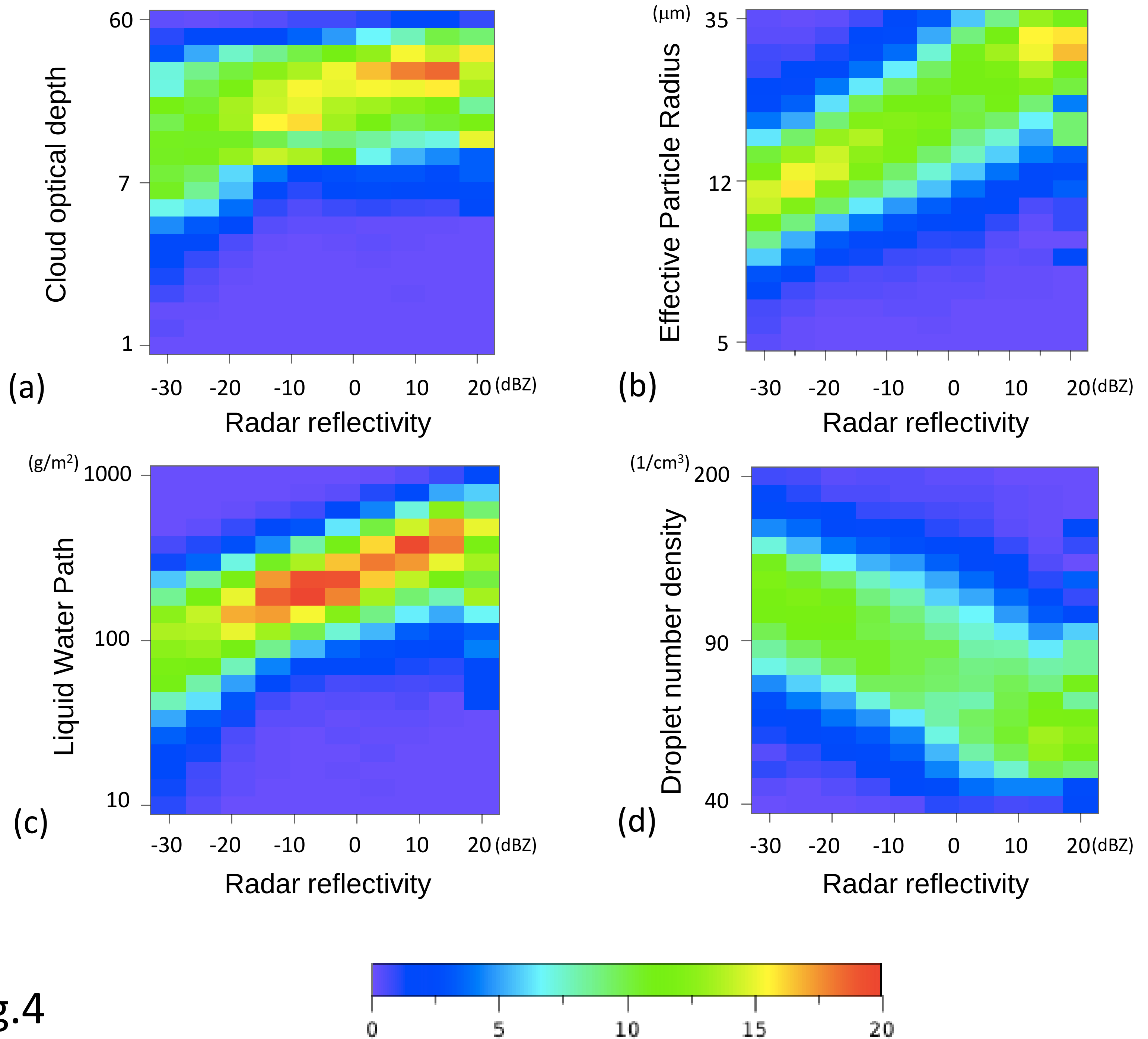

Cloud optical depth
60
7
1
(a)
-30 -20 -10 0 10 20 (dBZ)
Radar reflectivity
(μm)
Effective Particle Radius
35
12
5
(b)
-30 -20 -10 0 10 20 (dBZ)
Radar reflectivity
(g/m²)
Liquid Water Path
1000
100
10
(c)
-30 -20 -10 0 10 20 (dBZ)
Radar reflectivity
(1/cm³)
Droplet number density
200
90
40
(d)
-30 -20 -10 0 10 20 (dBZ)
Radar reflectivity
0 5 10 15 20

Fig.4

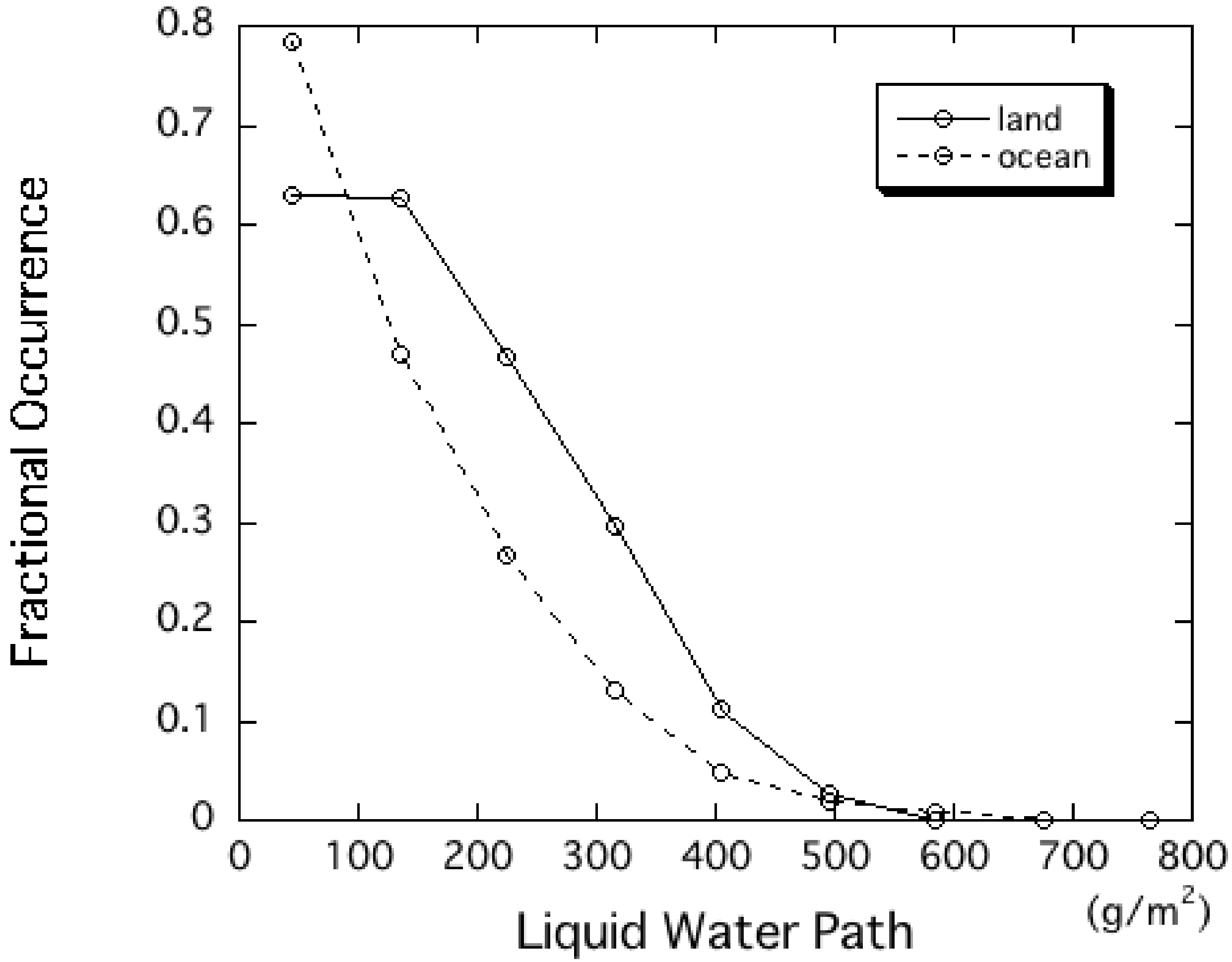
land
ocean
Fractional Occurrence
0.8
0.7
0.6
0.5
0.4
0.3
0.2
0.1
0
0
100
200
300
400
500
600
700
800
(g/m²)
Liquid Water Path

Fig.5 (a)

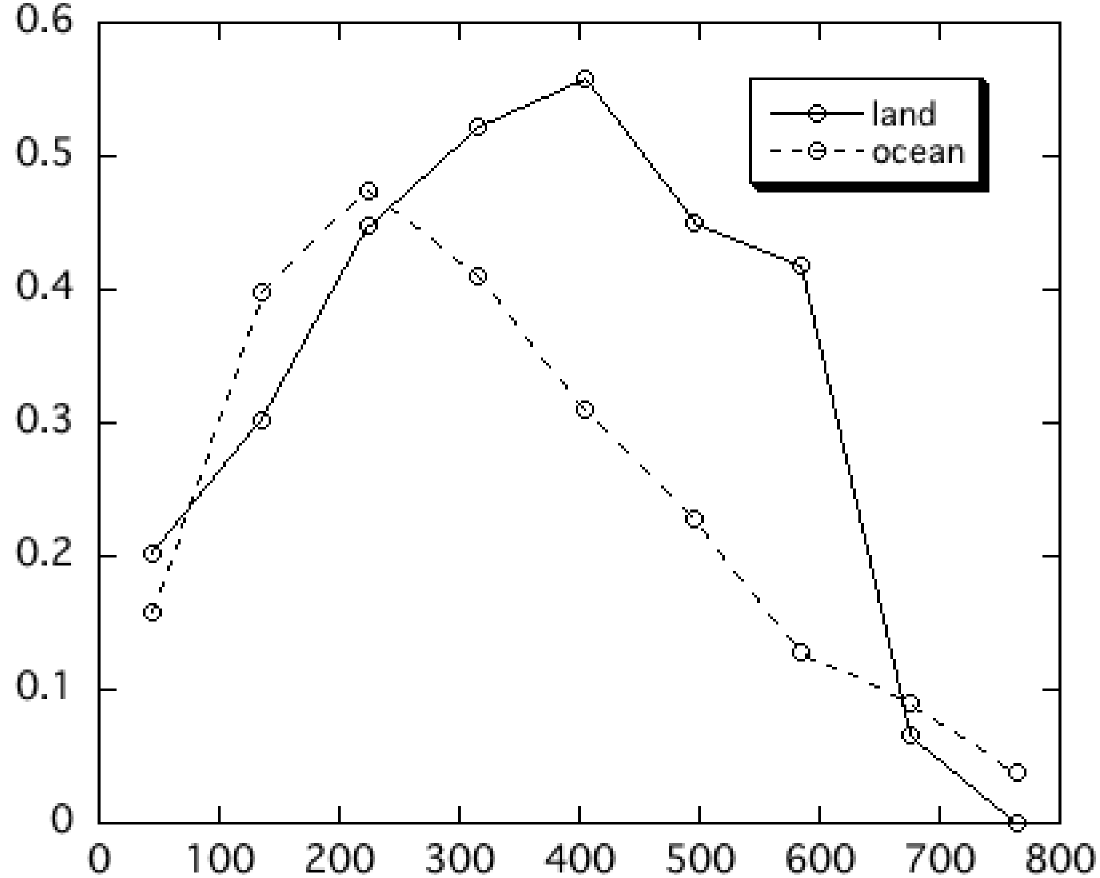

Fig.5 (b)

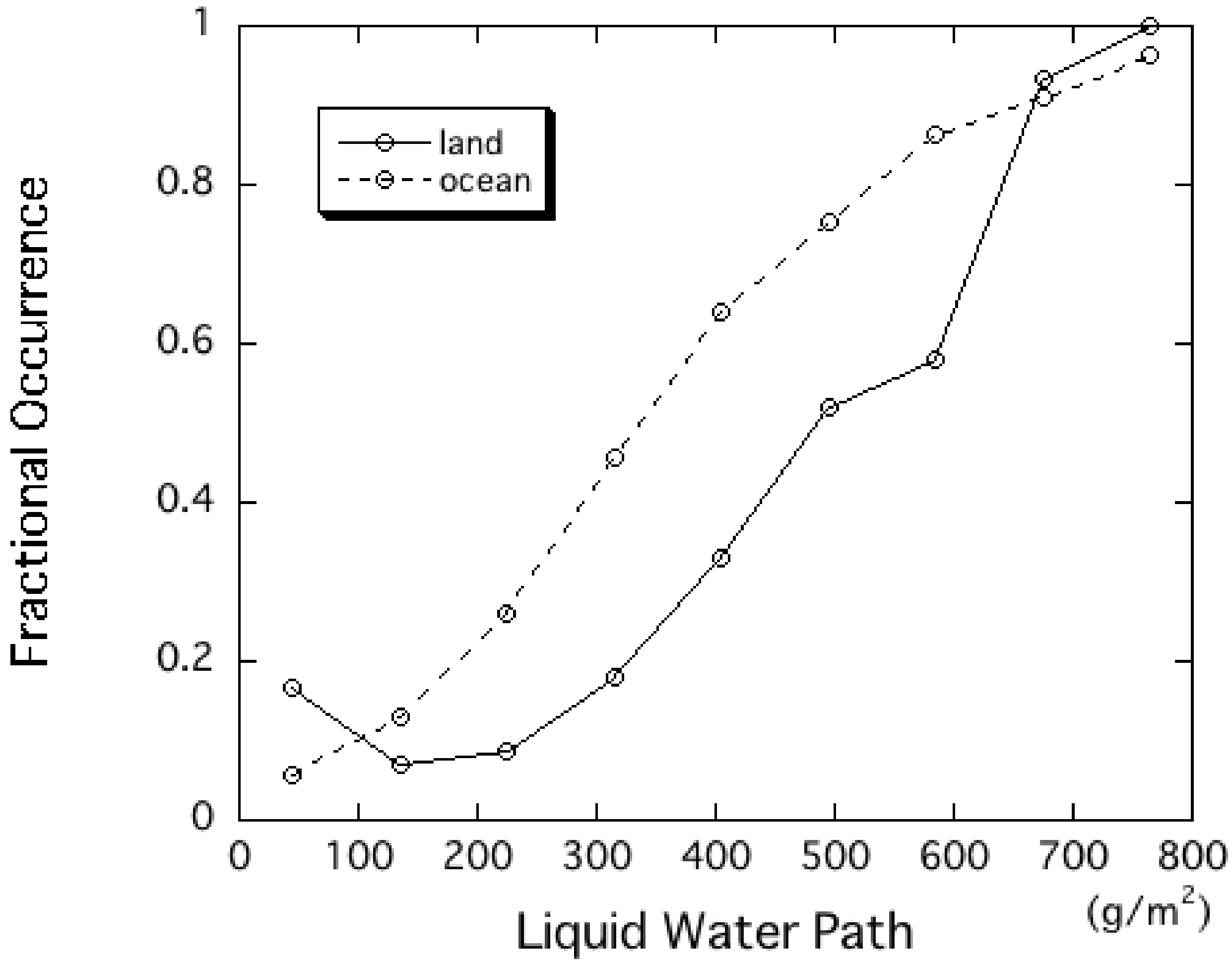

land
ocean
Fractional Occurrence
Liquid Water Path
(g/m2)
0
0.2
0.4
0.6
0.8
1
0
100
200
300
400
500
600
700
800

Fig.5 (c)

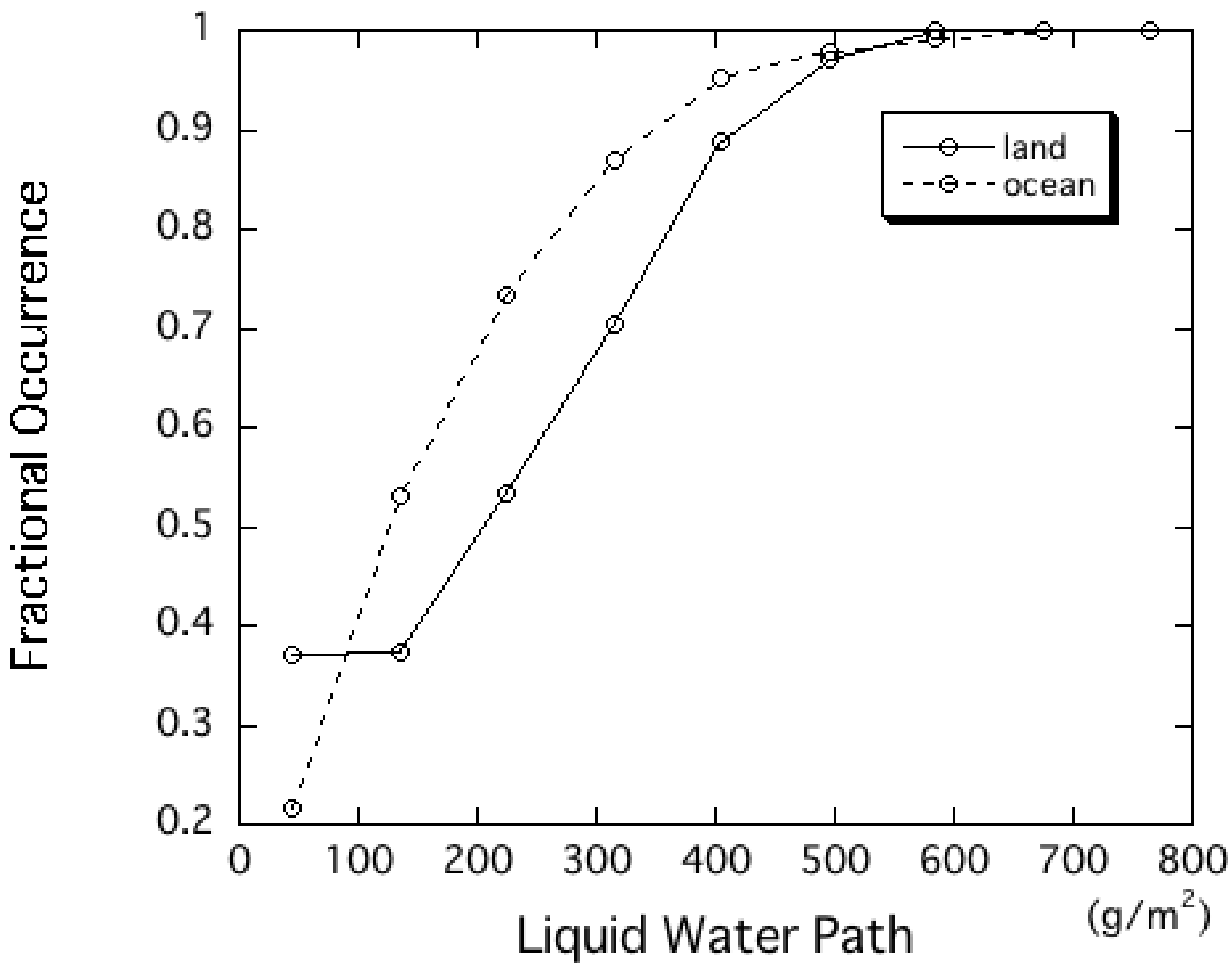

Fractional Occurrence
1
0.9
0.8
0.7
0.6
0.5
0.4
0.3
0.2
0
100
200
300
400
500
600
700
800
(g/m^2)
Liquid Water Path
land
ocean

Fig.5 (d)

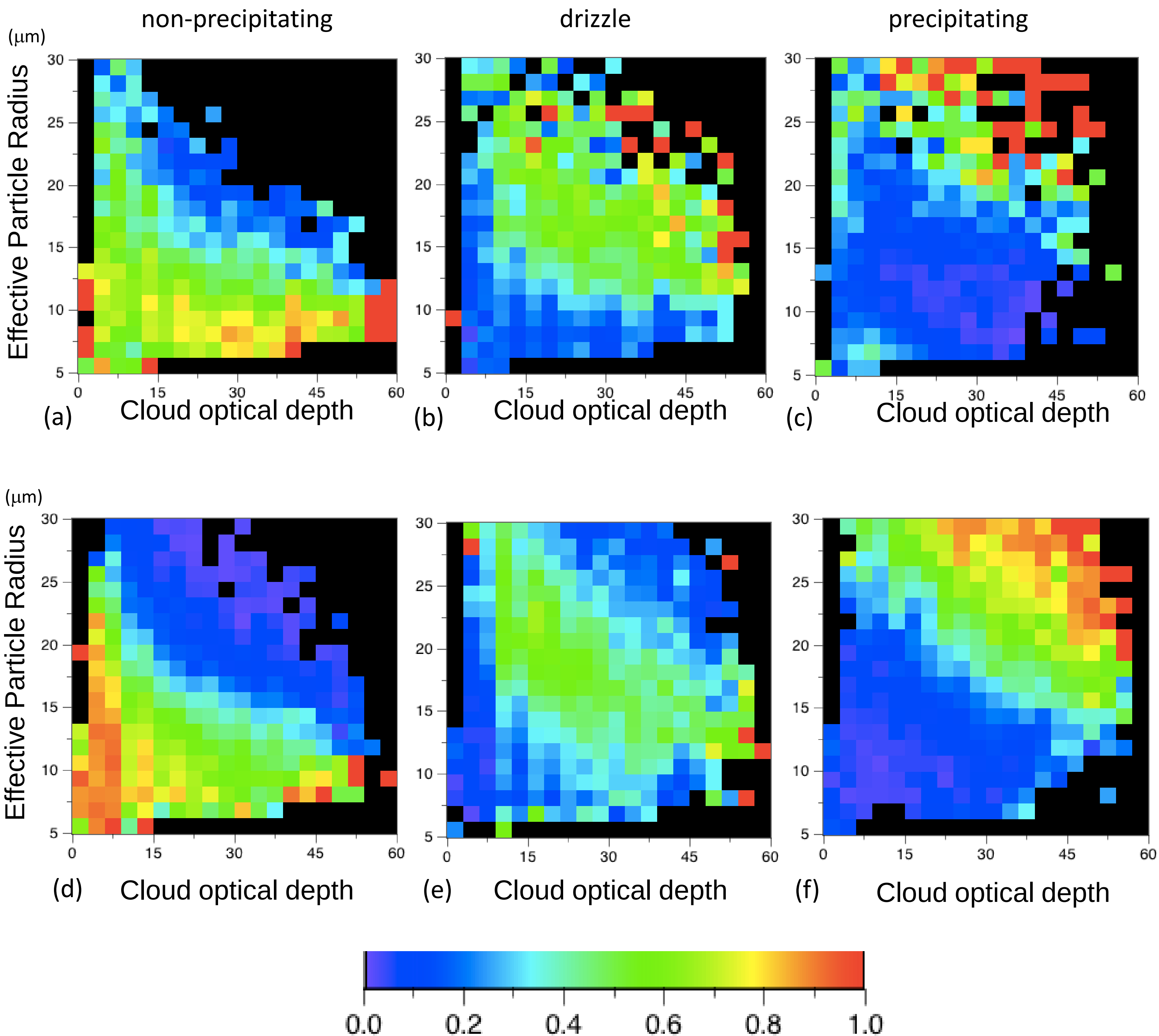
non-precipitating
drizzle
precipitating
(μm)
Effective Particle Radius
Cloud optical depth
(a)
(b)
(c)
(d)
(e)
(f)
0.0
0.2
0.4
0.6
0.8
1.0

Fig.6

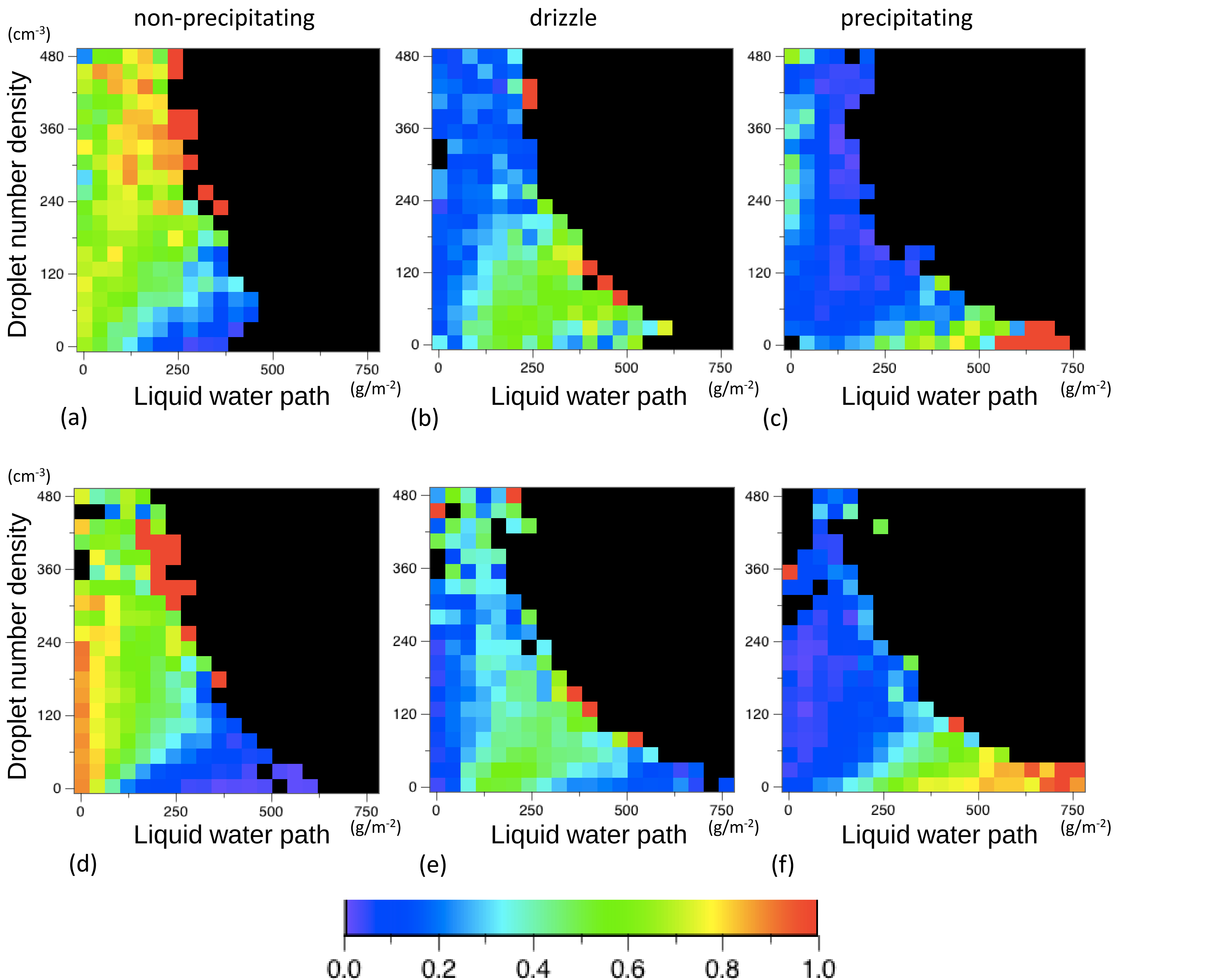

non-precipitating
drizzle
precipitating
(cm-3)
Droplet number density
480
360
240
120
0
0
250
500
750
(g/m-2)
Liquid water path
(a)
(b)
(c)
(d)
(e)
(f)
0.0
0.2
0.4
0.6
0.8
1.0

Fig.7

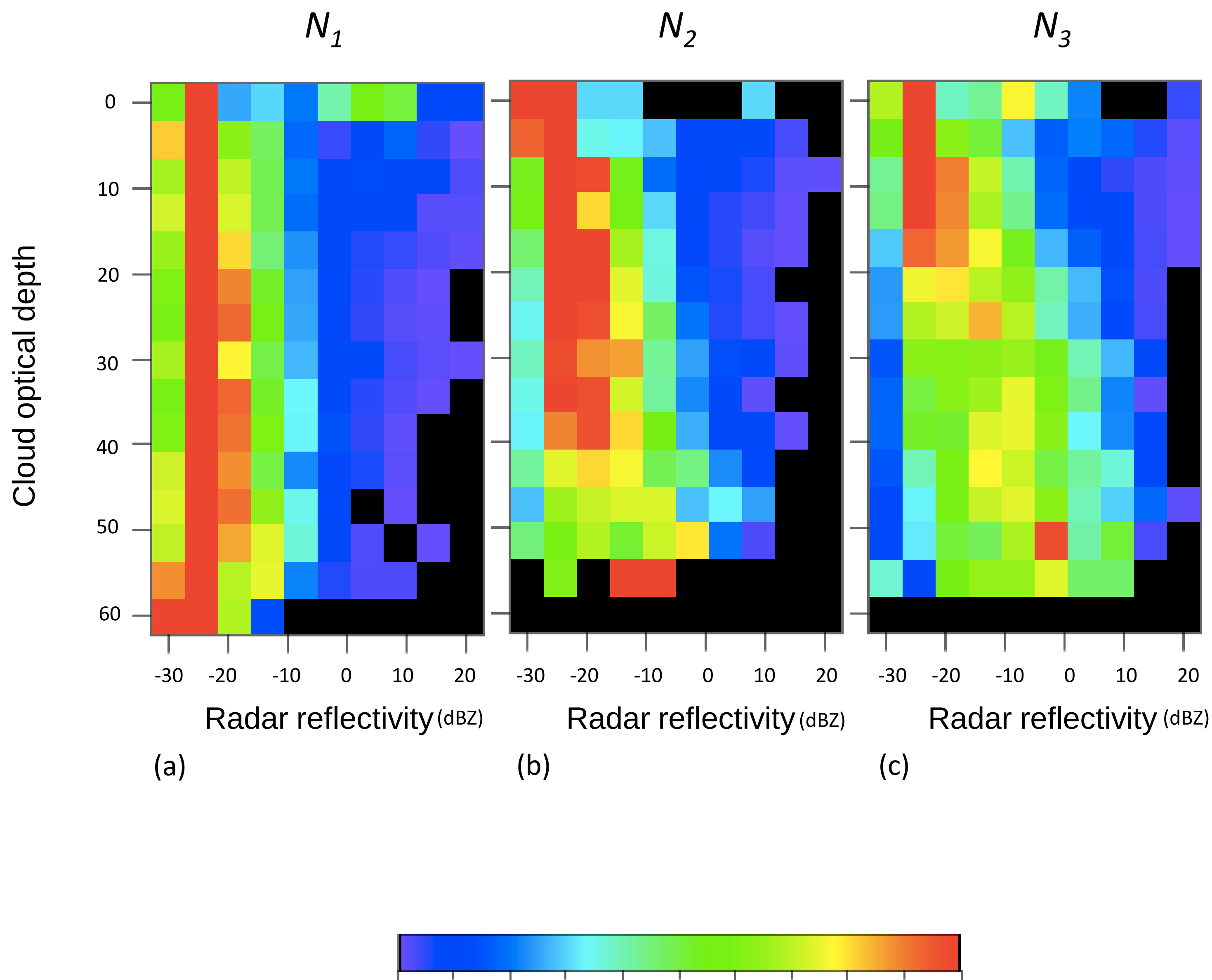

N1
N2
N3
Cloud optical depth
0
10
20
30
40
50
60
-30
-20
-10
0
10
20
Radar reflectivity (dBZ)
(a)
(b)
(c)
0
5
10
15
20
25

Fig.8

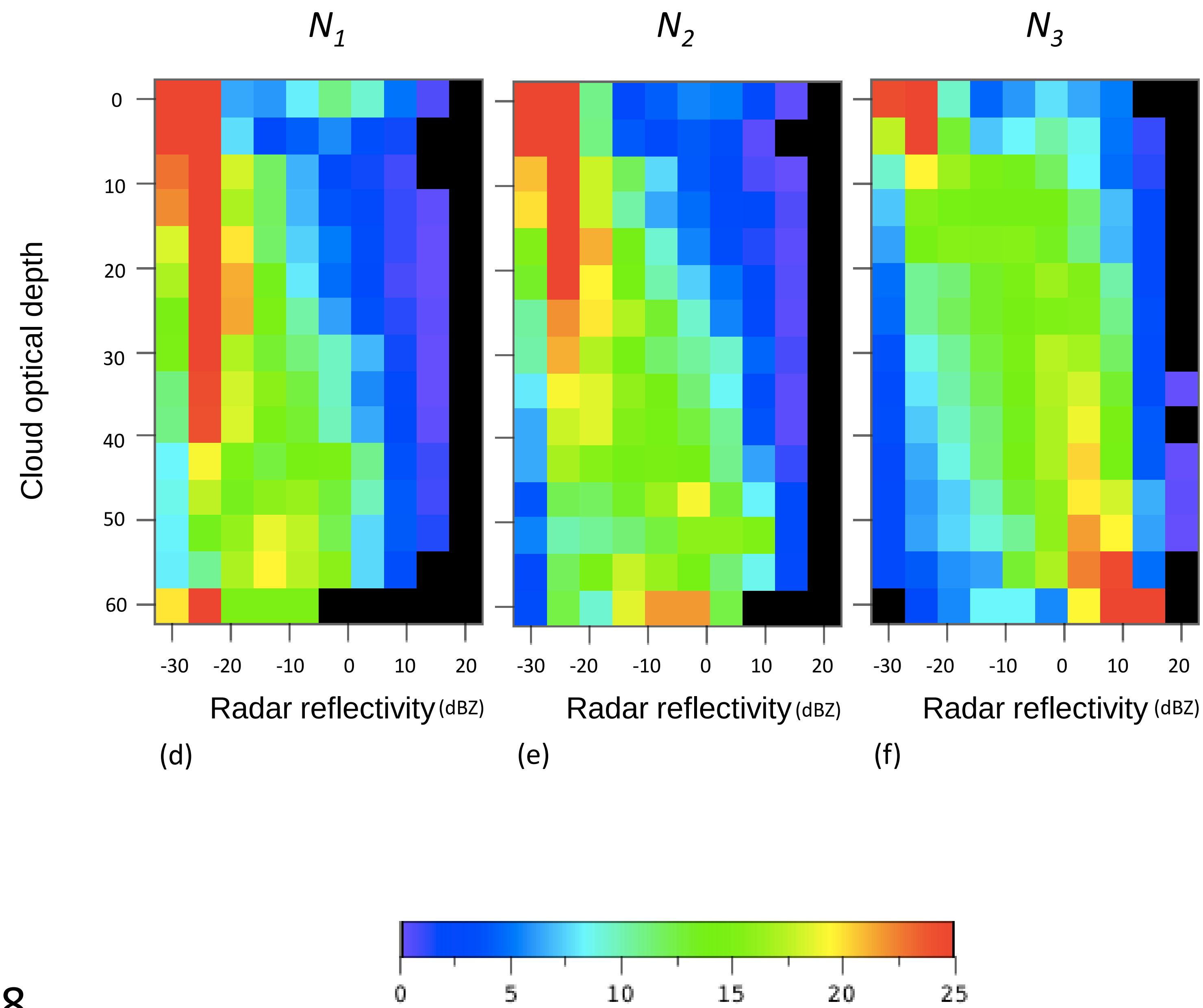

N_1
N_2
N_3
Cloud optical depth
0
10
20
30
40
50
60
-30
-20
-10
0
10
20
Radar reflectivity (dBZ)
(d)
(e)
(f)
0
5
10
15
20
25

Fig.8